

# Universal and scalable synthesis of photochromic single-atom catalysts for plastic recycling

Received: 20 March 2024

Accepted: 17 October 2024

Published online: 29 October 2024

Check for updates

Yu Liu<sup>1,6</sup>, Xuchun Wang<sup>1,2,6</sup>, Xiaodong Li<sup>3,6</sup>, Zuyang Ye<sup>4</sup>, Tsun-Kong Sham<sup>2</sup>, Panpan Xu<sup>5</sup>, Muhan Cao<sup>1</sup>, Qiao Zhang<sup>1</sup>, Yadong Yin<sup>4,7</sup>✉ & Jinxing Chen<sup>1,7</sup>✉

Metal oxide nanostructures with single-atomic heteroatom incorporation are of interest for many applications. However, a universal and scalable synthesis approach with high heteroatom concentrations represents a formidable challenge, primarily due to the pronounced structural disparities between  $M_{\text{hetero}}\text{-O}$  and  $M_{\text{sub}}\text{-O}$  units. Here, focusing on  $\text{TiO}_2$  as the exemplified substrate, we present a diethylene glycol-assisted synthetic platform tailored for the controlled preparation of a library of  $M_1\text{-TiO}_2$  nanostructures, encompassing 15 distinct unary  $M_1\text{-TiO}_2$  nanostructures, along with two types of binary and ternary composites. Our approach capitalizes on the unique properties of diethylene glycol, affording precise kinetic control by passivating the hydrolytic activity of heteroatom and simultaneously achieving thermodynamic control by introducing short-range order structures to dissipate the free energy associated with heteroatom incorporation. The  $M_1\text{-TiO}_2$  nanostructures, characterized by distinctive and abundant  $M\text{-O-Ti}$  units on the surface, exhibit high efficiency in photochromic photothermal catalysis toward recycling waste polyesters. This universal synthetic platform contributes to the preparation of materials with broad applicability and significance across catalysis, energy conversion, and biomedicine.

The concept of the asymmetric  $M_{\text{hetero}}\text{-O-M}_{\text{sub}}$  triple-atom structure centers on the creation of chemical bonds featured by localized asymmetry, achieved through the incorporation of heteroatoms,  $M_{\text{hetero}}$ , into metal oxide frameworks ( $M_{\text{sub}}\text{O}$ )<sup>1–3</sup>. This unique structural configuration holds significant promise for creating distinct atomic surroundings characterized by charge redistribution, lattice distortion, and notably, asymmetric oxygen vacancies denoted as  $M_{\text{hetero}}\text{-O}_v\text{-M}_{\text{sub}}$ <sup>4–8</sup>. Particularly noteworthy is the impact of  $M_{\text{hetero}}\text{-O-Ti}$  structures when  $M_{\text{sub}}\text{O}$  functions as a semiconductor, as exemplified by  $\text{TiO}_2$ , where they play a

pivotal role in introducing defect levels, enabling precise manipulation of the semiconductor's band structure<sup>9–12</sup>. The merits of constructing  $M_{\text{hetero}}\text{-TiO}_2$  structures are summarized in Fig. 1a. In pursuing an optimal  $M_{\text{hetero}}\text{-O-Ti}$  configuration, achieving atomic dispersion of  $M_{\text{hetero}}$  atoms within the  $\text{TiO}_2$  matrix becomes imperative. This specific configuration, denoted as  $M_1\text{-TiO}_2$ , is instrumental in maximizing the occurrence of  $M_{\text{hetero}}\text{-O-Ti}$  units while simultaneously eliminating  $M_{\text{hetero}}\text{-O-M}_{\text{hetero}}$  bonds. However, this favorable scenario is typically observed at low  $M_{\text{hetero}}$  concentrations<sup>13–18</sup>.

<sup>1</sup>Institute of Functional Nano & Soft Materials (FUNSOM), Jiangsu Key Laboratory for Carbon-Based Functional Materials & Devices, Soochow University, Suzhou 215123, China. <sup>2</sup>Department of Chemistry, University of Western Ontario, London, Ontario, ON N6A 5B7, Canada. <sup>3</sup>Max Planck Institute of Microstructure Physics, Weinberg 2, Halle 06120, Germany. <sup>4</sup>Department of Chemistry, University of California, Riverside, CA 92521, USA. <sup>5</sup>Advanced Materials Division, Suzhou Institute of Nano-Tech and Nano-Bionics, Chinese Academy of Sciences, Suzhou 215123, China. <sup>6</sup>These authors contributed equally: Yu Liu, Xuchun Wang, Xiaodong Li. <sup>7</sup>These authors jointly supervised this work: Yadong Yin, Jinxing Chen. ✉ e-mail: [yadong.yin@ucr.edu](mailto:yadong.yin@ucr.edu); [chenjinxing@suda.edu.cn](mailto:chenjinxing@suda.edu.cn)

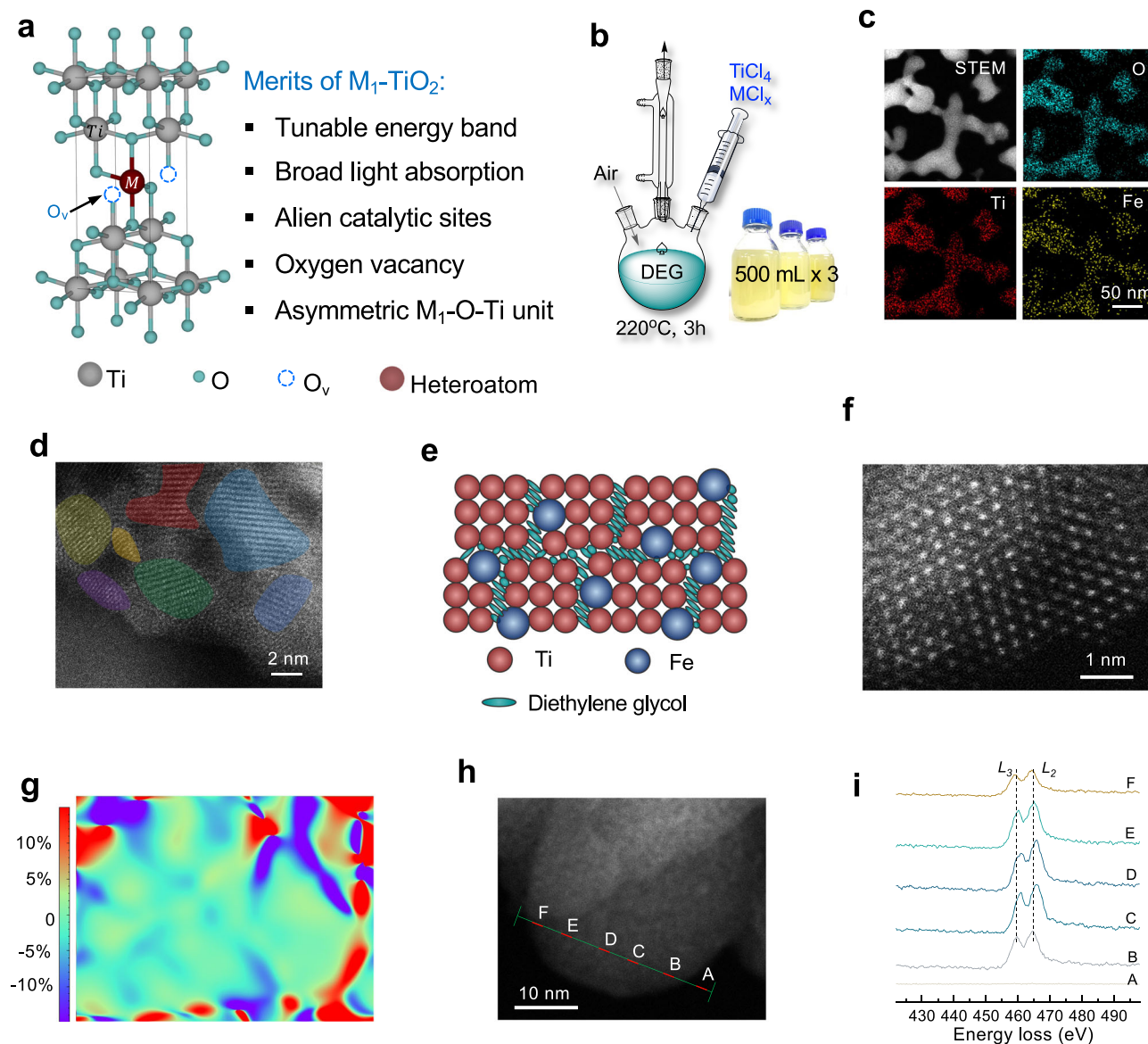


**Fig. 1 | Diethylene glycol (DEG)-assisted synthesis of  $\text{Fe}_1\text{-TiO}_2$  nanostructures.** **a** Merits of  $\text{Fe}_1\text{-TiO}_2$  nanostructures. **b** Schematic of the setup and reaction and digital image of the mass production of  $\text{Fe}_1\text{-TiO}_2/\text{H}_2\text{O}$  dispersion with a mass concentration of  $5 \text{ mg}\cdot\text{mL}^{-1}$ . **c** Scanning transmission electron microscopy and elemental maps of  $\text{Fe}_1\text{-TiO}_2$  nanostructures. **d** High-resolution transmission electron microscope image of  $\text{Fe}_1\text{-TiO}_2$  nanostructures. The colored regions represent crystal domains. **e** Schematic of  $\text{Fe}_1\text{-TiO}_2$  nanostructures. **f, g** Aberration-corrected

scanning transmission electron microscopy (AC-STEM) image and corresponding geometric phase analysis (GPA) image of crystal domain in  $\text{Fe}_1\text{-TiO}_2$ . **h, i** Electron energy loss spectroscopy (EELS) of  $\text{Fe}_1\text{-TiO}_2$  nanostructures performed on AC-STEM. The red dots correspond to the positions of the EELS line scan. The EELS spectra of  $\text{Ti-L}_{2,3}$  edge exhibits two groups of peaks,  $L_{3,1}$  and  $L_2$ , associated with electronic transitions from initial  $2p_{3/2}$  and  $2p_{1/2}$  core states to final  $3d$  states in the conduction band. Source data are provided as a Source Data file.

Numerous synthesis approaches have been devised to create  $\text{M}_1\text{-TiO}_2$ , including molten salt<sup>19</sup>, hot injection<sup>20</sup>, and pyrolysis<sup>21,22</sup>. However, current methodologies are often subject to stringent conditions, such as high temperatures, and are susceptible to oxygen and moisture. These constraints pose challenges to the scalability of production. Moreover, most of these approaches exhibit limitations in their universality, allowing for the doping of only a limited set of heteroatoms. Importantly, in  $\text{M}_1\text{-TiO}_2$  catalysts prepared by conventional doping systems, the heteroatoms are uniformly distributed within the  $\text{TiO}_2$  matrix, which loses many reaction sites in catalysis. Consequently, the universal and scalable synthesis of  $\text{M}_1\text{-TiO}_2$ , featuring high doping concentrations, continues to present a significant challenge, which primarily arises from two factors: (1) kinetic limitation: the formation rates of  $\text{M}_{\text{hetero}}\text{-O}$  and  $\text{Ti-O}$  units inherently exhibit disparities, creating a kinetic barrier to construct the atomically distributed

$\text{M}_{\text{hetero}}\text{-O-Ti}$  configuration; (2) thermodynamic limitation: as the concentration of  $\text{M}_{\text{hetero}}$  increases, the accumulation of lattice strain becomes progressively pronounced, thereby impeding the stabilization of  $\text{M}_1\text{-TiO}_2$  structures<sup>23,24</sup>.

Here, we present a versatile and scalable synthetic platform for creating  $\text{M}_1\text{-TiO}_2$  nanostructures with high heteroatom concentrations on the surface. The key to this strategy is the combination of kinetic control involving the passivation of hydrolysis activity of heteroatoms by diethylene glycol (DEG) and thermodynamic control by introducing short-range order structures to release free energy from lattice mismatch. As a result, this approach encompasses 15 distinct variations of  $\text{M}_1\text{-TiO}_2$  ( $\text{M} = \text{V}, \text{Cr}, \text{Mn}, \text{Fe}, \text{Co}, \text{Ni}, \text{Cu}, \text{Zn}, \text{Ga}, \text{Zr}, \text{Nb}, \text{Mo}, \text{Sn}, \text{Ta}, \text{and W}$ ), along with binary  $\text{Fe}_1\text{M}_1\text{-TiO}_2$  and ternary  $\text{Fe}_1\text{Co}_1\text{Cu}_1\text{-TiO}_2$  structures. Moreover, the  $\text{M}_1\text{-TiO}_2$  nanostructures, characterized by distinctive and abundant  $\text{M}_{\text{hetero}}\text{-O-Ti}$  units, exhibit exceptionally

efficient photochromic photothermal catalytic performance toward recycling waste polyesters. As an illustrative example, the photothermal recycling activity of Fe<sub>1</sub>-TiO<sub>2</sub> nanocatalyst surpasses that of undoped TiO<sub>2</sub> by a factor of 9.5. This heightened performance underscores the transformative potential of M<sub>1</sub>-TiO<sub>2</sub> in advancing sustainable and efficient processes for polyester recycling.

## Results

### Synthesis and structure information of Fe<sub>1</sub>-TiO<sub>2</sub>

We use the Fe<sub>1</sub>-TiO<sub>2</sub> nanostructure as an example to illustrate the synthetic process. This choice is primarily due to the widespread application of Fe<sub>1</sub>-TiO<sub>2</sub> nanostructure in various significant research areas such as photocatalysis, environmental treatment, energy conversion, and organic synthesis. Achieving controllable preparation of this nanostructure is expected to have direct applications in these fields. The Fe<sub>1</sub>-TiO<sub>2</sub> nanostructures were prepared by directly mixing FeCl<sub>3</sub> and TiCl<sub>4</sub> with DEG, and the solution was heated to 220 °C for 3 h. The resulting products were precipitated and washed with acetone. Notably, this synthesis method is resistant to air and humidity, making it highly suitable for large-scale production. Figure 1b and Supplementary Fig. 1 show a scaled-up reaction and mechanism with a total product volume of 1.5 L and a solid concentration of 5 mg·mL<sup>-1</sup>.

Figure 1c shows a scanning transmission electron microscopy (STEM) image illustrating the typical morphology of Fe<sub>1</sub>-TiO<sub>2</sub> nanostructures, along with elemental maps demonstrating the uniform distribution of O, Ti, and Fe elements. Aberration-corrected scanning transmission electron microscopy (AC-STEM, Fig. 1d and Supplementary Fig. 2) reveals that Fe<sub>1</sub>-TiO<sub>2</sub> is polycrystalline with massive grain boundaries. The low crystallinity and anatase phase of Fe<sub>1</sub>-TiO<sub>2</sub> is further confirmed by X-ray diffraction (XRD, Supplementary Fig. 3)<sup>25</sup>. We suggest that this grain boundary arises from the formation of a spatial barrier by the DEG on the surface, which converts the structure from long-range order into short-range order, thus mitigating the free energy increase due to the introduction of heteroatoms (Fig. 1e)<sup>26</sup>. Thermogravimetric analysis (TGA, Supplementary Fig. 4) of Fe<sub>1</sub>-TiO<sub>2</sub> shows a total mass loss of 8.3% at around 300 °C (above the boiling point of DEG), where the departing components may be attributed to the surface bonded DEG<sup>27</sup>. To quantitatively identify the strain accumulation in the lattice, geometric phase analysis (GPA) based on a high-resolution transmission electron microscope (HRTEM) image was acquired (Fig. 1f, g, see detailed methodologies in the Supplementary). The amorphous area exhibits a maximum strain, while less lattice strain (less than 3.5%) is observed in the crystal domain<sup>28</sup>.

Electron energy loss spectroscopy (EELS) performed on AC-STEM was utilized to probe the local chemical and electronic properties of Ti in Fe<sub>1</sub>-TiO<sub>2</sub> nanostructures. Figure 1h illustrates the position (green line) of the EELS line scan. As the line scan progresses from “B” to “F”, the energy loss of the Ti-L<sub>3</sub> edge values ranges from 459.7 to 460.9, 461.2, 460.2, and 459.1 eV (Fig. 1i). This finding indicates a higher concentration of Ti<sup>3+</sup> species near the outer layer of Fe<sub>1</sub>-TiO<sub>2</sub> nanostructures. We inferred that the TiO<sub>2</sub> in the inner core was formed earlier and had enough time to condense, producing the perfect Ti-O-Ti structure. Conversely, the freshly formed shell layer exhibited more defects.

X-ray absorption near-edge structure (XANES) analysis further elucidates the electronic state of Ti sites in Fe<sub>1</sub>-TiO<sub>2</sub> nanostructures (Fig. 2a). A comparison with TiO<sub>2</sub> nanostructures, prepared using the same method but lacking the addition of the FeCl<sub>3</sub> precursor, reveals a weakened whiteness intensity in Fe<sub>1</sub>-TiO<sub>2</sub>. This disparity signifies more unoccupied valence states of Ti in Fe<sub>1</sub>-TiO<sub>2</sub> than TiO<sub>2</sub> nanostructures<sup>29–31</sup>. The threshold energy of Ti in the Fe<sub>1</sub>-TiO<sub>2</sub> is lower than that of TiO<sub>2</sub>, demonstrating that its lower valence state (Supplementary Table 1)<sup>32–34</sup>.

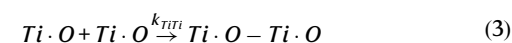
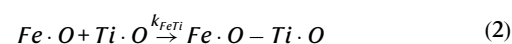
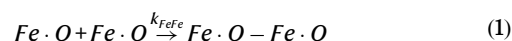
To gain a comprehensive understanding of the electronic states and local structure of Fe species in Fe<sub>1</sub>-TiO<sub>2</sub>, X-ray absorption fine

structures, including XANES and extended X-ray absorption fine structure (EXAFS), were collected at the Fe K-edge. The threshold energy of the Fe<sub>1</sub>-TiO<sub>2</sub> absorption edge is located between that of Fe<sub>2</sub>O<sub>3</sub> and Fe foil, demonstrating that its valence state is lower than Fe (III) of Fe<sub>2</sub>O<sub>3</sub> but higher than Fe (0) of Fe foil (Fig. 2b). By plotting the energy threshold position, which increases with the oxidation state (Supplementary Fig. 5), the precise oxidation state of Fe in the Fe<sub>1</sub>-TiO<sub>2</sub> is calculated to be +2.7. Figure 2c shows Fourier-transformed EXAFS spectra of samples and references. A solitary peak is observed around 1.58 Å in Fe<sub>1</sub>-TiO<sub>2</sub>, which is attributed to the Fe-O scattering path, similar to Fe<sub>2</sub>O<sub>3</sub> and Fe<sub>3</sub>O<sub>4</sub>. Notably, the Fe-(O)-Fe scattering path is absent in the case of Fe<sub>1</sub>-TiO<sub>2</sub>, indicating that Fe is atomically dispersed in the TiO<sub>2</sub> matrix. Notably, when the feed ratio of FeCl<sub>3</sub> is as high as 25.00 at.%, the Fe atomic proportion of the product measured by inductively coupled plasma optical emission spectroscopy (ICP-OES) is 3.87 at.%, and the Fe atoms in the product still exist in the form of single atoms, which positions it at the upper level of current capabilities (Supplementary Table 2).

To further verify the single-site characteristic, we conducted wavelet transform (WT) on EXAFS spectra at Fe K-edge (Fig. 2d). Notably, a sole intensity peak is evident at  $k = 4.59 \text{ \AA}^{-1}$  and  $R = 1.57 \text{ \AA}$  in the case of Fe<sub>1</sub>-TiO<sub>2</sub>. This specific pattern is attributed to the Fe-O scattering path, substantiated by its resemblance to that observed in Fe<sub>3</sub>O<sub>4</sub> ( $k = 4.54 \text{ \AA}^{-1}$ ,  $R = 1.53 \text{ \AA}$ ). Conversely, the absence of analogous patterns in Fe<sub>1</sub>-TiO<sub>2</sub> at  $k = 6.07 \text{ \AA}^{-1}$ ,  $R = 2.81 \text{ \AA}$  (as observed in Fe<sub>3</sub>O<sub>4</sub>) and  $k = 6.37 \text{ \AA}^{-1}$ ,  $R = 2.58 \text{ \AA}$  (as seen in Fe<sub>2</sub>O<sub>3</sub>, Supplementary Figs. 6–8) effectively rules out the presence of oxide clusters. Furthermore, the analysis provides compelling evidence for the single-site dispersion of Fe within the Fe<sub>1</sub>-TiO<sub>2</sub> structure. The fitting results reveal that Fe within Fe<sub>1</sub>-TiO<sub>2</sub> exhibits coordination with -3.33 oxygen atoms, with an interatomic distance of 2.08 Å between Fe and its neighboring oxygen atom (Supplementary Table 3). This unsaturated coordination environment is anticipated to profoundly influence its catalytic performance<sup>35</sup>.

### Kinetic analysis

The formation of TiO<sub>2</sub> nanostructures is analogous to the polymerization process<sup>36</sup>. Therefore, we define the parameter of reactivity ratio to theoretically predict the prerequisites for the synthesis of M<sub>1</sub>-TiO<sub>2</sub>. With  $Fe \cdot O$  and  $Ti \cdot O$  representing the two units, their growth modes can be divided into four types as follows:



Here  $k$  represents the reaction rate constant. The reactivity ratio ( $r$ ) is the rate constant ratio of the self-growth to the cross-growth ( $r_{Fe} = k_{FeFe}/k_{FeTi}$ ;  $r_{Ti} = k_{TiTi}/k_{TiFe}$ ). The growth of nanoparticles can be considered an equilibrium process. The composition of  $Fe \cdot O$  in the product is a function of the feed ratio of  $Fe \cdot O$  in the reactant, and the reactivity ratio is the main parameter affecting the relationship between these two.

We then show the theoretical interpretation of the typical reactivity ratio values. (1) The case of  $r_{Fe} = r_{Ti} = 1$  means that the self-growth and cross-growth probabilities of the two precursors are exactly the same, and the ratio of the two atoms in the product is consistent with that of the reactant. The products have chemical

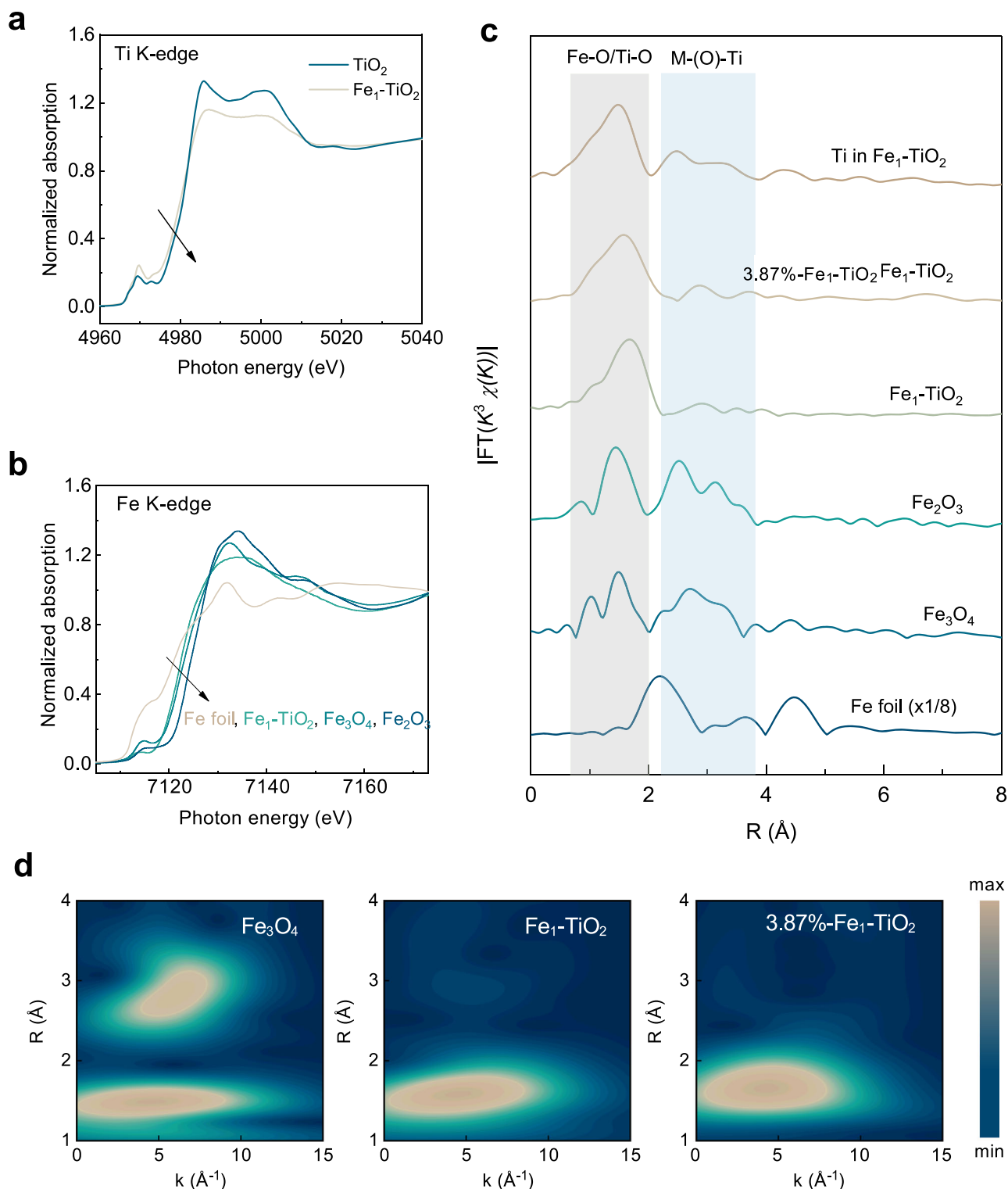


**Fig. 2 | X-ray absorption spectra (XAS) studies of  $\text{Fe}_1\text{-TiO}_2$  nanostructures.**

**a, b** Normalized X-ray absorption near-edge structure (XANES) spectra of  $\text{Fe}_1\text{-TiO}_2$  and references at Ti K-edge (**a**) and Fe K-edge (**b**). **c** Normalized Fourier transform-extended X-ray absorption fine structure (FT-EXAFS) spectra of  $\text{Fe}_1\text{-TiO}_2$ , 3.87 at.%  $\text{Fe}_1\text{-TiO}_2$ , and  $\text{Fe}_3\text{O}_4$ . The orange and blue regions represent the Fe-O/Ti-O and M-

(O)-Ti scattering path, respectively. **d** Wavelet transform-extended X-ray absorption fine structure (WT-EXAFS) contour plots of  $\text{Fe}_1\text{-TiO}_2$ , 3.87 at.%  $\text{Fe}_1\text{-TiO}_2$ , and  $\text{Fe}_3\text{O}_4$ . The maximum and minimum values on the contour scales represent the magnitude of the WT signal, with the units expressed in arbitrary units. Source data are provided as a Source Data file.

structures of  $\text{Fe}\cdot\text{O}-\text{Fe}\cdot\text{O}$  and  $\text{Fe}\cdot\text{O}-\text{Ti}\cdot\text{O}$ . This model is not preferred to prepare  $\text{Fe}_1\text{-TiO}_2$  nanostructures (Fig. 3a). (2) The second case is  $r_{\text{Fe}}=r_{\text{Ti}}=0$ , where the self-growth for the two precursors is forbidden, and only cross-growth can be allowed. The atoms are

arranged in an alternating structure (Fig. 3b). Although this model provides an ideal  $\text{Fe}\cdot\text{O}-\text{Ti}\cdot\text{O}$  unit, it is thermodynamically unstable because of evident lattice strain. (3) The third typical structure can be obtained by combining the above two cases, where the  $r_{\text{Ti}}\gg 1$

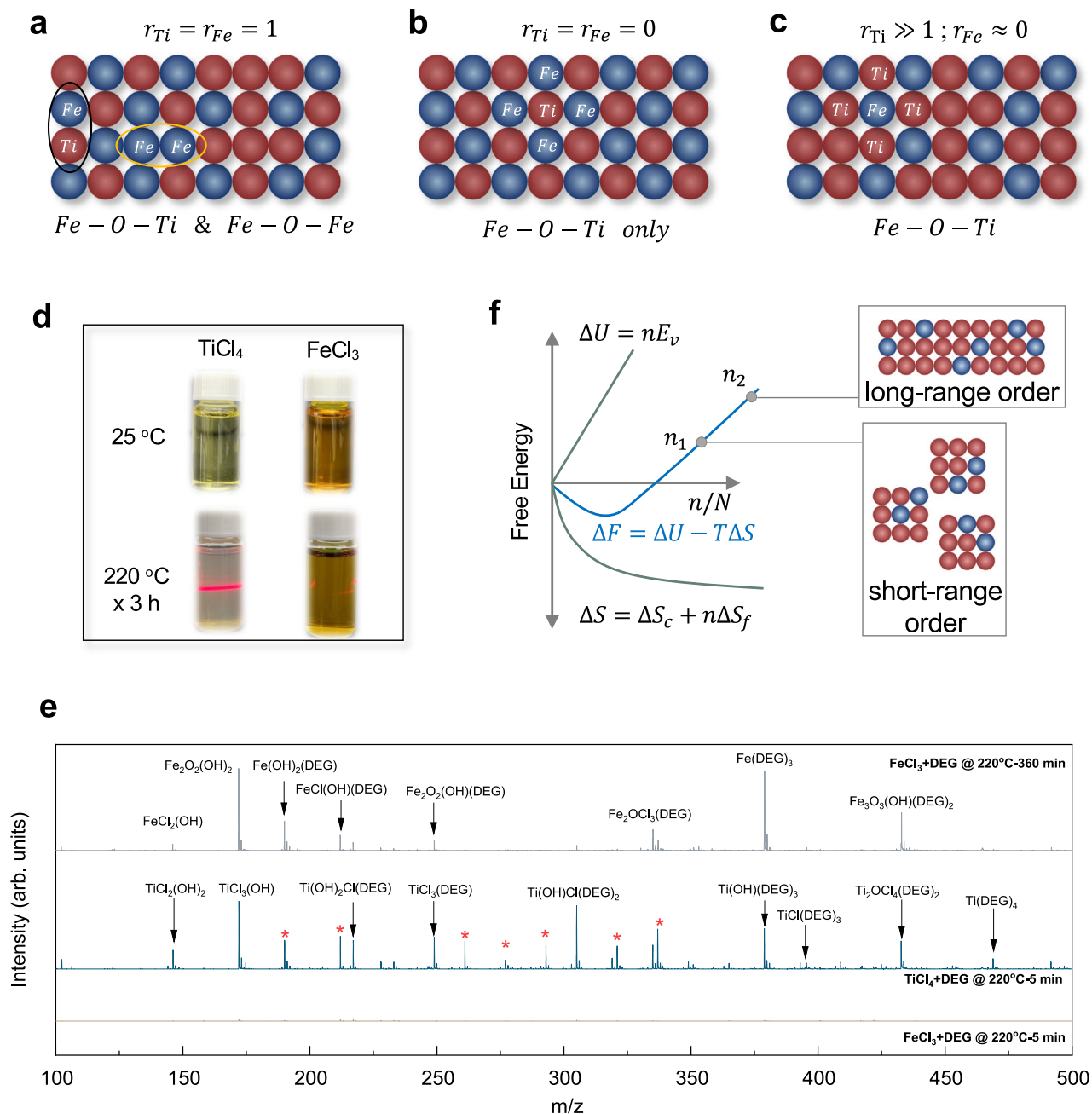


**Fig. 3 | Reaction mechanism of diethylene glycol (DEG)-assisted synthesis.**

**a–c** Schematic showing the effect of reactivity on atoms configuration in the product. **d** Digital images of  $\text{TiCl}_4/\text{DEG}$  and  $\text{FeCl}_3/\text{DEG}$  solutions at 25 and 220 °C. **e** Matrix-assisted laser desorption-ionization-time of flight mass spectrometry of

the coordination structures between  $\text{TiCl}_4/\text{FeCl}_3$  and DEG. **f** Plots of free energy  $F$ , internal energy  $U$ , and entropy  $S$  against defect concentration. Source data are provided as a Source Data file.

( $k_{\text{Ti}, \text{Ti}} \gg k_{\text{Ti}, \text{Fe}}$ ) and  $r_{\text{Fe}} \approx 0$  ( $k_{\text{Fe}, \text{Fe}} \ll k_{\text{Fe}, \text{Ti}}$ ). The  $\text{Ti} \cdot \text{O} - \text{Ti} \cdot \text{O}$  and  $\text{Fe} \cdot \text{O} - \text{Ti} \cdot \text{O}$  structures co-exist in the product, with the former configuration dominating and  $\text{Fe} \cdot \text{O} - \text{Fe} \cdot \text{O}$  missing, analogous to the single-atom alloy (Fig. 3c).

The third possibility manifests itself solely in cases where the hydrolysis rate of the Fe precursor is much slower than that of its Ti counterpart, and this fact was confirmed by the experimental observation. Upon introducing  $\text{TiCl}_4$  into DEG, the solution changed to light yellow (Fig. 3d). As the reaction progressed at a temperature of 220 °C for 3 h, a conspicuous Tyndall effect emerged, signifying the formation of abundant  $\text{TiO}_2$  nanoparticles. The hydrolysis of  $\text{FeCl}_3$  under the same conditions showed no Tyndall effect throughout the observation

period. These results suggest that the important influence of DEG-bound atoms on hydrolysis kinetics.

The coordination structures of these chemical species were elucidated using matrix-assisted laser degradation/ionization-time of flight (MALDI-TOF) mass spectrometry (MS). The samples for MALDI-TOF MS were prepared by mixing either 0.2 mL of  $\text{TiCl}_4$  or 295 mg of  $\text{FeCl}_3$  with 20 mL of DEG at a temperature of 220 °C, allowing the mixture to react for 5 min. Figure 3e illustrates the presence of Ti-DEG complexes, including  $\text{TiCl}_3(\text{DEG})$ ,  $\text{Ti}(\text{OH})\text{Cl}(\text{DEG})_2$ ,  $\text{Ti}(\text{OH})(\text{DEG})_3$ ,  $\text{TiCl}(\text{DEG})_3$ , and  $\text{Ti}(\text{DEG})_4$ . These findings confirm that DEG undergoes ligand exchange with chlorine during the synthesis. The plausibility of ligand exchange occurring at  $\text{Ti}^{4+}$  sites arises from the presence of an

unoccupied  $3d$  orbital within the central Ti atom. In this context, when an oxygen atom from DEG with an available lone electron pair draws near to the Ti atom, these electrons can be introduced into the vacant orbital, leading to the establishment of a five-coordinate intermediate with  $sp^3d$  hybridization<sup>37,38</sup>. Subsequently, the expulsion of H and Cl in the form of HCl facilitates a transition from  $sp^3d$  hybridization to  $sp^3$  hybridization. Of significant note, we have also observed that DEG manifests within certain Ti–O oligomers (marked with an asterisk, exemplified by  $Ti_2O_2Cl_4(DEG)_2$ ). The emergence of these configurations implies the potential presence of DEG ligands within the ultimate product, which aligns seamlessly with the outcomes deduced from our TGA curve.

In contrast, the 5-min reaction of the  $FeCl_3$ -DEG sample did not show any detectable Fe-DEG species, strongly supporting the understanding that  $FeCl_3$  has difficulty forming a complex with DEG. When the reaction was extended to a duration of 3 h, various Fe-DEG complexes, including  $Fe(OH)_2(DEG)$ ,  $FeCl(OH)(DEG)$ ,  $Fe_2O_2(OH)(DEG)$ , and  $Fe(DEG)_3$ , were formed. We hypothesized that the different coordination behaviors of DEG towards  $TiCl_4$  and  $FeCl_3$  stem from variations in the strength of the Ti–Cl and Fe–Cl bonds. Specifically, the Ti–Cl bond possesses a lower bond dissociation energy, aligning with the known instability of  $TiCl_4$ . Consequently, this inherent instability facilitates the formation of a stable Ti-DEG complex through the readily disintegrating Ti–Cl bond. The kinetic analysis has established the feasibility of DEG-assisted synthesis for  $Fe_1-TiO_2$ .

### Thermodynamic insights into the crystal stability

The critical role played by DEG in stabilizing crystal structures was highlighted from a thermodynamic perspective. Incorporating heteroatoms into  $TiO_2$  usually introduces point defects, resulting in an elevation of the internal energy of the crystal and a subsequent reduction in its thermodynamic stability. Simultaneously, introducing defects increases disorder in the atomic arrangement, thus altering the vibrational frequency of the surrounding atoms<sup>39</sup>. Consequently, changes occur in both group and vibrational entropy, contributing to an increase in crystal entropy and a subsequent enhancement in the crystal's thermodynamic stability. These two opposing factors establish an equilibrium concentration of point defects in the crystal at a specific temperature, which can be calculated using thermodynamic principles. We consider the case of vacancies and outline the calculation procedure as:

$$F = U - TS \quad (5)$$

where  $F$  represents the system's free energy,  $U$  signifies the internal energy,  $S$  encompasses the overall entropy encompassing both group entropy ( $S_c$ ) and vibrational entropy ( $S_f$ ), and  $T$  denotes the absolute temperature. In a crystal comprised of  $N$  atoms,  $E_v$  represents the energy required to generate these vacancies. When the crystal accommodates  $n$  vacancies, the internal energy of the crystal increases by  $nE_v$ . Additionally, incorporating a vacancy induces a change in the crystal's group entropy, denoted as  $\Delta S_c$ , and a corresponding alteration in the vibrational entropy of  $n\Delta S_f$ . Consequently, the modification in the free energy is delineated as:

$$\Delta F = nE_v - T(\Delta S_c + n\Delta S_f) \quad (6)$$

According to statistical thermodynamics and Stirling approximation, the above formula can be written as (see details in the Supplementary Information):

$$\Delta F = n(E_v - T\Delta S_f) - kT[(N+n)\ln(N+n) - N\ln N - n\ln n] \quad (7)$$

Figure 3f depicts the schematic relationship between free energy and periodic quantities. Reaching the equilibrium concentration

greatly increases the crystal's free energy as the heteroatom doping levels and periodic lengths increase. This outcome suggests a significant role played by the short-range ordered structure in liberating the crystal's free energy provoked by the introduction of heteroatoms.

The above analysis suggests that DEG plays a crucial role in the fabrication of  $Fe_1-TiO_2$ , influencing both the thermodynamics and kinetics of the process. DEG regulates the hydrolysis rates of Fe and Ti precursors, ensuring synchronized precipitation and promoting a uniform dispersion of Fe atoms within the  $TiO_2$  framework. In addition, DEG facilitates the conversion of the long-range ordered structure into one with short-range order, thereby mitigating the free energy increase associated with heteroatom incorporation. These intertwined effects contribute to the successful creation of  $Fe_1-TiO_2$  nanostructures.

### Library synthesis

Our strategy is versatile and applicable to synthesizing various heteroatom-doped  $TiO_2$  nanostructures. We have successfully synthesized 15 types of unary  $M_1-TiO_2$  nanostructures ( $M = V, Cr, Mn, Fe, Co, Ni, Cu, Zn, Ga, Zr, Nb, Mo, Sn, Ta, W$ , Fig. 4a and Supplementary Figs. 9–16). This methodology can also be extended to incorporate multiple types of atoms in  $TiO_2$ , exemplified by  $Fe_1Mo_1-TiO_2$  and  $Fe_1Co_1Cu_1-TiO_2$ . To investigate the local chemical structure and geometric features of the heteroatoms, we have chosen  $Ni_1-TiO_2$ ,  $Fe_1Mo_1-TiO_2$ , and  $Fe_1Co_1Cu_1-TiO_2$  as representative systems. The elemental mapping displayed in Fig. 4b–d unequivocally depicts the presence of heteroatoms across all samples. Moreover, EXAFS (Fig. 4e) and XANES data (Supplementary Figs. 17–21 and Table 3) indicate that all heteroatoms in the  $Ni_1-TiO_2$ ,  $Fe_1Mo_1-TiO_2$ , and  $Fe_1Co_1Cu_1-TiO_2$  samples manifested exclusively as M–O–Ti scattering paths, devoid of any indications of M–(O)–M scattering paths. Additionally, the aberration-corrected high-angle annular dark-field scanning transmission electron microscopy (AC-HAADF-STEM) of the  $Fe_1Mo_1-TiO_2$  sample suggested that the Mo atoms were atomically dispersed in the  $TiO_2$  matrix (Supplementary Fig. 22). This compelling revelation strongly supports the inference that heteroatoms are single-atomically incorporated into the lattice of  $TiO_2$ . The heteroatom doping in the  $TiO_2$  lattice usually generates oxygen vacancies and  $Ti^{3+}$  species<sup>40</sup>. These defects can modulate the energy band structure, enhancing light absorption of  $TiO_2$ <sup>41</sup>. The band engineering through heteroatom doping was summarized in Supplementary Figs. 23–39, providing a material library with promising prospects for future applications<sup>42</sup>.

An ideal method to synthesize  $M_1-TiO_2$  should achieve precise control over multiple dopants while adaptable to various elements. ICP-OES analysis revealed that, for a given precursor, the M/Ti ratio exhibited a linear relationship with the corresponding value in the resulting product (Fig. 4f), underscoring the capability for finely tuning the heteroatom concentration. Figure 4g summarizes the M/Ti ratios in products, highlighting the versatility and precision attainable through this synthesis approach in tailoring single-atom doping levels for diverse elemental compositions. Importantly, this method facilitates single-atom doping with a high content of heteroatom on the surface of the  $TiO_2$  matrix, which improves the density of catalytic sites. As shown in Supplementary Fig. 40, X-ray photoelectron spectroscopy (XPS) depth profiling reveals structural information at different depths. The Fe–Ti atomic ratio on the catalyst surface is 13.7%, which decreases as the etching depth increases. Specifically, the ratio decreases to 7.8% at an etching depth of ~3 nm.

It should be pointed out that our strategy encounters limitations when incorporating metal precursors with high reduction potentials. For instance, when employing  $RuCl_3$  as a precursor, we observed a preferential reduction of  $Ru^{3+}$  cations to  $Ru^0$ , even in the presence of air. This phenomenon stems from DEG's potent reduction capability at elevated temperatures. Once  $Ru^0$  is formed, it impedes the assimilation of Ru species into the structural units of  $TiO_2$ , as depicted in

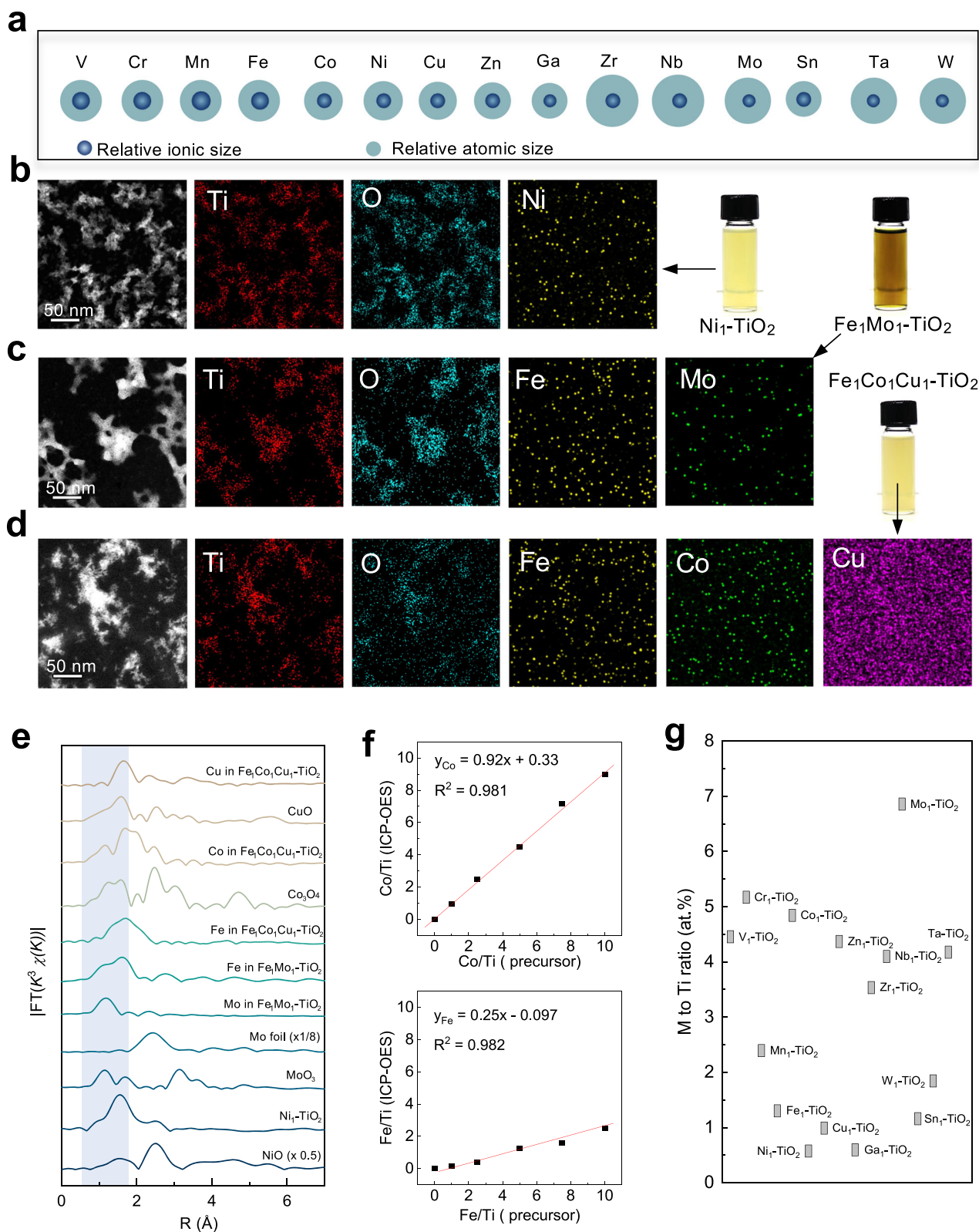


**Fig. 4 | Library synthesis.** **a** Relative ionic size and atomic size of doped ions. **b–d** Scanning transmission electron microscopy images and elemental maps of  $\text{Ni}_1\text{-TiO}_2$ ,  $\text{Fe}_1\text{Mo}_1\text{-TiO}_2$ ,  $\text{Fe}_1\text{Co}_1\text{Cu}_1\text{-TiO}_2$  nanostructures. **e** Normalized Fourier transform extended X-ray absorption fine structure spectra of  $\text{Ni}_1\text{-TiO}_2$ ,  $\text{Fe}_1\text{Mo}_1\text{-TiO}_2$ ,  $\text{Fe}_1\text{Co}_1\text{Cu}_1\text{-TiO}_2$  nanostructures and references. The blue region represents the M-

O/Ti-O scattering path. **f** Plot of the Fe/Ti and Co-Ti ratios in the products against the M/Ti ratios in the precursors in a typical synthesis. **g** Summarized M/Ti atomic ratios in various  $\text{M}_1\text{-TiO}_2$  nanostructures with feeding ratios all of 5 at.%. Source data are provided as a Source Data file.

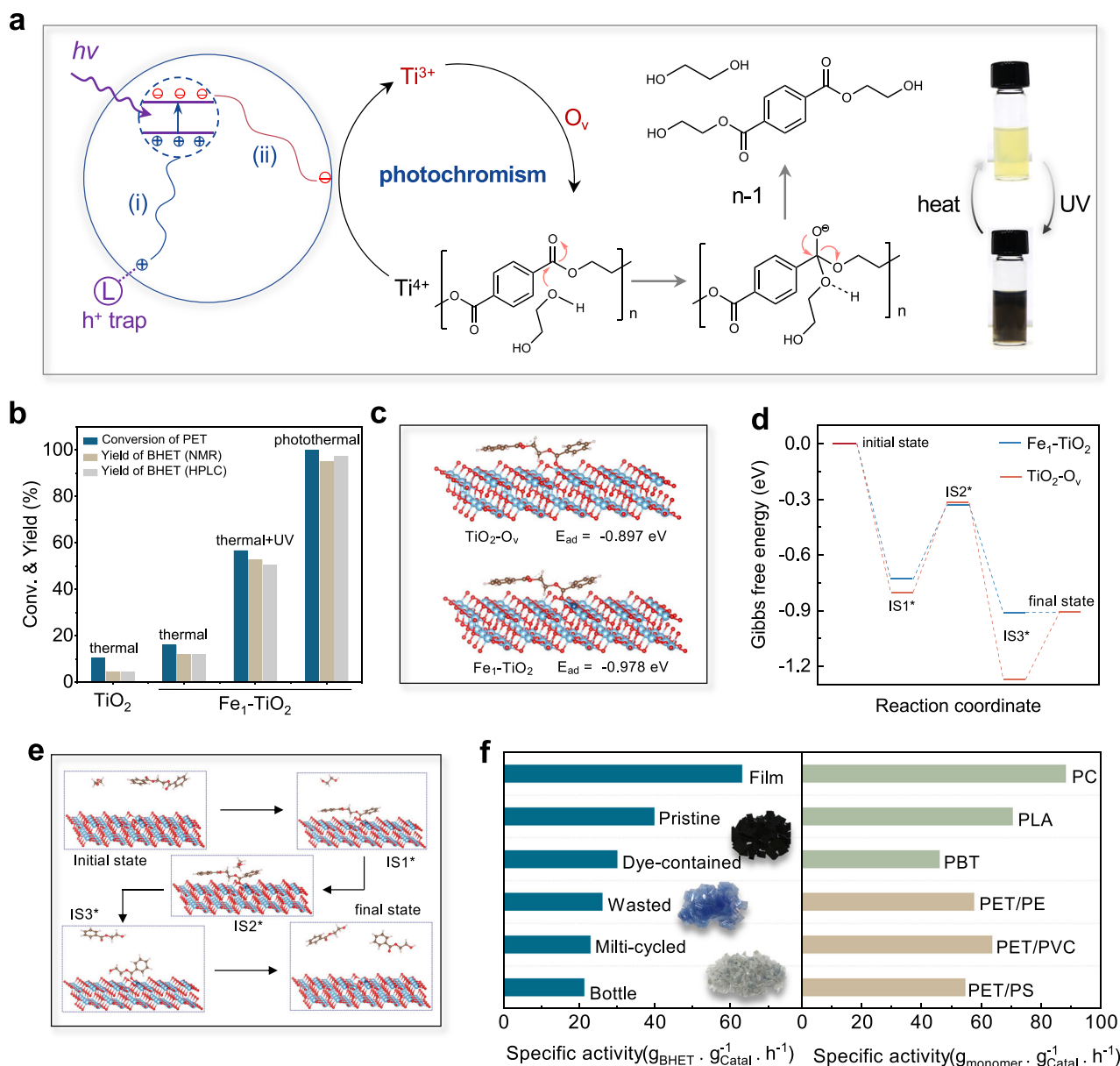


**Fig. 5 | Photothermal catalysis.** **a** Photochromism mechanism and photothermal catalytic processes of polyethylene terephthalate (PET) glycolysis. **b** PET conversion and bis(2-hydroxyethyl) terephthalate (BHET) yield at various conditions. In thermal and thermal + UV conditions the reactor was placed in an oil bath to keep a temperature of 190 °C. The UV light intensity is 0.052 W·cm<sup>-2</sup>. In photothermal, the reactor was irradiated by simulated sunlight (0.52 W·cm<sup>-2</sup>). **c** The adsorbed model and adsorption energy of ethylene glycol dibenzoate (EGD) on TiO<sub>2</sub>-O<sub>v</sub> and Fe<sub>1</sub>-TiO<sub>2</sub> slabs. Atom key: Ti (light blue), Fe (navy), O (red), C (green), H (white). **d**, **e** The

calculated Gibbs free energy profiles and the intermediate models of photothermal catalytic PET glycolysis on TiO<sub>2</sub>-O<sub>v</sub> and Fe<sub>1</sub>-TiO<sub>2</sub> slabs. Atom key: Ti (light blue), Fe (navy), O (red), C (green), H (white). **f** The specific activities of Fe<sub>1</sub>-TiO<sub>2</sub> toward various polyesters. Insets are the images of dyed PET lunch boxes (black), PET bottles (blue), and multi-cycled PET flakes (gray). About 20 mg of Fe<sub>1</sub>-TiO<sub>2</sub> catalysts, 2 g of ethylene glycol, and 0.5 g of various polyester flakes were added to a sealed quartz reactor with a thermocouple inserted to keep a temperature of 190 °C. Source data are provided as a Source Data file.

Supplementary Fig. 41. Similar observations emerged with the use of PdCl<sub>2</sub>, RhCl<sub>3</sub>, and IrCl<sub>3</sub> as precursors, as documented in Supplementary Figs. 42–44. Therefore, the difficulty in reducing the precursor is a necessary condition for the formation of single-atom structures. In this regard, the DEG-assisted synthesis strategy may be further extended to efficiently prepare metal nanoparticle-supported catalysts.

### Photothermal catalytic polyester recycling

Photochromic materials hold significant potential for applications in catalysis. For instance, Li and colleagues reported on photochromic Bi<sub>2</sub>WO<sub>6-x</sub>/amorphous BiOCl (p-BWO) nanosheets, which showed blue coloration upon light irradiation. The existence of abundant W(VI)O<sub>6-x</sub> units served as the sites for the fast and continuous consumption of

photogenerated electrons, thereby effectively facilitating the separation of electron-hole pairs<sup>43</sup>. Similarly, Hyeon and collaborators have developed a reversible and synergistic photo-activation process involving individual copper atoms anchored on the TiO<sub>2</sub> surface, thereby enabling the reversible regulation of the macroscopic and optoelectronic properties of TiO<sub>2</sub><sup>40</sup>. We have previously reported the remarkable potential of DEG-modified TiO<sub>2</sub> nanostructures for polyethylene terephthalate (PET) recycling<sup>44</sup>. Upon exposure to ultraviolet (UV) light, TiO<sub>2</sub> generates electron-hole pairs (Fig. 5a). Subsequently, the holes migrate to the catalyst's surface, where they are captured by the chemically bonded DEG. Concurrently, the photogenerated electrons prompt the reduction of Ti<sup>4+</sup> to Ti<sup>3+</sup> (Supplementary Fig. 45) and the formation of oxygen vacancies (O<sub>v</sub>). The presence of Ti<sup>3+</sup> imparts a

distinct black hue to the catalyst, extending its sunlight absorption to the visible range and enhancing heat generation. The  $O_v$  acts as the active site to facilitate the activation of the oxygen in the carbonyl group of PET, inducing a positive charge on the carbon atom within the carbonyl group. Subsequently, EG assumes the role of a nucleophile, initiating an attack on the polarized carbonyl group. This interaction sets in motion a comprehensive transesterification cycle, ultimately cleaving the PET chain and forming bis(2-hydroxyethyl) terephthalate (BHET).

Here, we carried out a comparative analysis of the photochromic characteristics between  $TiO_2$  and  $Fe_1-TiO_2$  nanostructures. The  $Fe_1-TiO_2$  catalyst was chosen as an example mainly based on its top catalytic activity (Supplementary Fig. 46). Upon exposure to UV light, the  $TiO_2$  dispersion changed from light yellow to gray and ultimately to black over 70 seconds (Supplementary Fig. 47). In contrast, the color alteration in the  $Fe_1-TiO_2$  nanostructure solution, with an equivalent mass concentration, occurs more rapidly (<30 s), suggesting their enhanced photochromic capacity. After exposure to full-spectrum sunlight, the  $Fe_1-TiO_2$  dispersion demonstrates remarkable performance in photothermal conversion. When subjected to simulated sunlight at an intensity of  $0.52 \text{ W}\cdot\text{cm}^{-2}$ , a solution containing 1 wt% of  $Fe_1-TiO_2$  could be rapidly heated to  $190^\circ\text{C}$  within only 30 min (Supplementary Fig. 48). This property is highly desirable for enhancing the efficiency of photothermal catalytic polyester recycling.

We initially investigated the thermal catalytic efficacy of both  $TiO_2$  and  $Fe_1-TiO_2$  in the absence of light. Their catalytically active sites consist predominantly of  $O_v$  and originate from the intrinsic defects within the materials. As illustrated in Fig. 5b,  $Fe_1-TiO_2$  demonstrates a catalytic activity 1.5 times higher than  $TiO_2$ , indicating that introducing Fe heteroatoms can boost catalytic performance. When exposed to simulated sunlight, the catalysts turned black as they were activated by the UV photons, triggering significant photothermal conversion that could drive the catalytic reaction without any external heating source. Notably, by fine-tuning the light intensity, we successfully managed to modulate the reaction temperature in photothermal catalysis, aligning it with thermal catalysis conditions. This meticulous control has resulted in a significant improvement in catalytic performance, with the PET conversion increased from 16.0% to 100%, marking an approximately 6.3-fold increase (Supplementary Fig. 49), and the BHET yield also saw an increase from 12.0 to 95.1% (7.9-fold) (Supplementary Figs. 50, 51). Supplementary Table 4 lists the performance of previously reported catalytic systems for the glycolysis of PET. Notably, under similar reaction conditions, the  $Fe_1-TiO_2$  catalyst provided comparable or even higher space-time yields. Further, to evaluate the contribution of UV activation to the catalytic performance, we introduced UV irradiation into the thermal catalytic process and observed a sharp enhancement in catalytic activity with increasing light intensity. This substantial augmentation may be ascribed to photoactivation, which results in the generation of supplementary active sites<sup>44,45</sup>. In addition, photogenerated electrons may activate oxygen to generate reactive oxygen species (ROS), which in turn affects the glycolysis process. To this end, we first compared the catalytic activity of the catalyst in air and nitrogen atmosphere. As shown in Supplementary Fig. 52, the results under nitrogen are similar to those observed under ambient air conditions, which preliminarily rules out the contribution of ROS.

To delve into the catalytic mechanism, we embarked on a theoretical investigation of the catalytic mechanism of  $Fe_1-TiO_2$  catalysts in the photothermal-catalyzed PET glycolysis reaction using density functional theory (DFT) calculations. We began by constructing crystal structure models of  $Fe_1-TiO_2$  and  $TiO_2$  catalysts with oxygen vacancies ( $TiO_2-O_v$ ), as illustrated in Supplementary Fig. 53. Subsequently, we calculated the charge density differences on the surface of these crystal structures (Supplementary Fig. 54). In  $TiO_2-O_v$  catalysts, electrons predominantly cluster around Ti atoms, while electrons tend to

concentrate near Fe atoms in  $Fe_1-TiO_2$  catalysts. To further corroborate these observations, we conducted a Bader charge analysis. This analysis confirmed distinct differences in the charge density distribution of atoms surrounding the oxygen vacancies between the  $Fe_1-TiO_2$  catalysts and  $TiO_2-O_v$  (Supplementary Fig. 55).

The adsorption of PET molecules on the catalyst surface is an important step in PET glycolysis. Therefore, we further investigated the adsorption characteristics of PET on both  $Fe_1-TiO_2$  and  $TiO_2-O_v$  catalysts. To simplify the complexity of the calculations, we chose the widely used ethylene glycol dibenzoate (EGD) with a similar structure to PET as a model molecule to calculate the adsorption energies ( $E_{ad}$ ). As shown in Fig. 5c, the  $E_{ad}$  value of EGD adsorbed on  $Fe_1-TiO_2$  catalysts ( $-0.978 \text{ eV}$ ) is much lower than that adsorbed on  $TiO_2-O_v$  catalysts ( $-0.897 \text{ eV}$ ), which suggests that Fe- $O_v$ -Ti sites are more preferred for the adsorption of EGDs compared to Ti- $O_v$ -Ti sites. This preference stems from the modulation of the electronic states of the surrounding atoms by the incorporation of iron single atoms. Therefore, it can be inferred that the addition of heteroatoms to  $TiO_2-O_v$  alters the interaction between the  $O_v$  active site and the EGD molecule.

Then, we conducted Gibbs free energy calculations for each elementary step in the glycolysis of EGD on  $Fe_1-TiO_2$  and  $TiO_2-O_v$  catalysts (supplementary Table 5). As illustrated in Fig. 5d, the glycolysis mechanism is deconstructed into two transition states: initially, an EGD molecule adsorbs on the electron-deficient  $O_v$  of the catalysts (IS1'), which activates the carbonyl group of EGD. Subsequently, the hydroxyl group of EG undergoes a nucleophilic attack on the carbonyl group to generate another covalent bond (IS2'). Two 2-hydroxyethyl benzoate (2-HB) molecules are formed (IS3') and then desorbed from the oxygen vacancy. The calculations reveal that in both catalysts, the rate-determining step (RDS) involves the nucleophilic attack of EG to the carbonyl group of the adsorbed EGD. With the  $Fe_1-TiO_2$  catalysts, the nucleophilic attack of ethylene glycol required only 0.40 eV to surpass the IS2', whereas the  $TiO_2-O_v$  catalysts necessitate 0.48 eV. These findings suggest that the adsorption and activation of PET can be effectively enhanced at the Fe- $O_v$ -Ti sites, thereby accelerating catalytic performance.

The  $Fe_1-TiO_2$  catalyst showed efficient recycling performance towards a diverse range of PET materials, including pristine PET, packaging film, bottles, dye-containing lunch boxes, multi-recycled waste, and bottle waste sourced from Taihu Lake (Fig. 5e). Of particular significance, the catalytic efficiency towards PET film reached a specific activity of  $63.1 \text{ g}_{\text{monomer}}\cdot\text{g}_{\text{catal}}^{-1}\cdot\text{h}^{-1}$ , a value markedly exceeding the activity observed for additive-free pristine PET ( $39.7 \text{ g}_{\text{monomer}}\cdot\text{g}_{\text{catal}}^{-1}\cdot\text{h}^{-1}$ ). This improved performance can be attributed, at least in part, to the larger surface area of the film. It is important to note that impurities and additives inherent in post-consumer PET materials impart a slight compromise to the catalytic efficacy. Moreover, the landscape of plastic waste typically encompasses an assortment of mixed polymers, adding additional complexity. Notwithstanding this challenge, the  $Fe_1-TiO_2$  catalyst consistently exhibited its competence when faced with physical blends of PET and diverse plastics such as polyvinyl chloride (PVC), polyethylene (PE), and polystyrene (PS). These findings underscore the  $Fe_1-TiO_2$  catalyst's versatility and resilience in addressing authentic PET waste scenarios, reaffirming its potential for real-world applicability. Additionally, the recycled BHET showed high purity (Supplementary Fig. 56).

Our method facilitates the doping of single-atom with a high content of heteroatom on the surface of  $TiO_2$  matrix, which features abundant of accessible active sites, which endows it with the capability to depolymerize a wide spectrum of substrates. The investigations showcased the noteworthy activity exhibited by  $Fe_1-TiO_2$  across a diverse array of polyester types. For instance, we have observed substantial catalytic rates for materials such as polylactic acid (PLA, reaching  $70.5 \text{ g}_{\text{monomer}}\cdot\text{g}_{\text{catal}}^{-1}\cdot\text{h}^{-1}$ ), polycarbonate (PC, achieving  $88.2 \text{ g}_{\text{monomer}}\cdot\text{g}_{\text{catal}}^{-1}\cdot\text{h}^{-1}$ ), and polybutylene adipate terephthalate (PBAT,

attaining  $46.1 \text{ g}_{\text{monomer}} \cdot \text{g}_{\text{catal}}^{-1} \cdot \text{h}^{-1}$ ). Importantly, this broad spectrum of substrate applicability does not in any way undermine the central role of PET recycling<sup>46</sup>. Furthermore, our catalyst exhibited no significant decline in activity over extended operational periods of up to 25 h (Supplementary Figs. S7–S9), demonstrating exceptional stability. This remarkable durability inspires confidence for industrial use, making it a reliable and robust material for real-world applications.

## Discussion

The DEG-assisted synthesis strategy makes it possible to design and prepare single heteroatom-doped TiO<sub>2</sub> nanostructures with structural and band complexities that were previously unachievable. This simple, universal, and scalable route enables the synthesis of a library of diverse M<sub>1</sub>-TiO<sub>2</sub> nanostructures under mild conditions with broad substrate applicability. Mechanism studies reveal that the DEG can guide the single-atomic growth of heteroatoms through both thermodynamic and kinetic means. The resulting Fe<sub>1</sub>-TiO<sub>2</sub> nanostructures exhibit solid performance as photothermal catalysts for polyester recycling reactions, showcasing the potential of this synthetic route for downstream catalytic applications. Furthermore, using benchtop chemistry and standard laboratory glassware, the synthetic strategy can be extended to prepare both simple and complex single-atom nanostructures, such as high-entropy metal oxides.

## Methods

### Materials and characterizations

All chemicals were employed without additional purification. See detailed material information and characterization methods in the supplementary text.

### Synthesis of M<sub>1</sub>-TiO<sub>2</sub> nanostructures

In a standard procedure, 0.4 mL of TiCl<sub>4</sub> (3.64 mmol) and metal chloride (0.18 mmol) were combined with 40 mL of diethylene glycol (DEG), followed by heating to 50 °C and maintained for 5 min to ensure complete dissolution of TiCl<sub>4</sub> and metal chloride. Subsequently, 0.4 mL of H<sub>2</sub>O was introduced to hydrolyze TiCl<sub>4</sub> and metal chloride, facilitating the simultaneous formation of metal-DEG complexes. The M<sub>1</sub>-TiO<sub>2</sub> nanostructures were synthesized by heating at 220 °C for 3 h in an air atmosphere. Finally, the products were precipitated with acetone and collected via centrifugation. The resulting solids underwent four washes with acetone to eliminate excess DEG before being redispersed in ethylene glycol (EG), yielding a solid content of 20 mg·mL<sup>-1</sup> of M<sub>1</sub>-TiO<sub>2</sub>. The feeding ratios of various metal chlorides were referenced in Supplementary Table 6.

### Preparation of noble metal (NM) nanoparticles on TiO<sub>2</sub> (NM = Ru, Rh, Pd, Ir)

In a typical procedure, 0.4 mL of TiCl<sub>4</sub> (3.64 mmol) and noble metal chloride (0.18 mmol) were introduced into 40 mL of DEG, followed by heating to 50 °C and maintaining for 5 min to ensure complete dissolution of TiCl<sub>4</sub> and the noble metal chloride. Subsequently, 0.4 mL of H<sub>2</sub>O was added to facilitate the hydrolysis of TiCl<sub>4</sub> and the noble metal chloride, leading to the simultaneous formation of metal-DEG complexes. The NM-TiO<sub>2</sub> nanostructures were synthesized by heating at 220 °C for 3 h in an air atmosphere. Finally, the products were precipitated with acetone and collected via centrifugation. The resulting solids underwent four washes with acetone to remove excess DEG.

### Photochromic measurements

To assess the photochromic properties of Fe<sub>1</sub>-TiO<sub>2</sub> nanostructures, 0.5 mL of the aforementioned Fe<sub>1</sub>-TiO<sub>2</sub> nanostructure dispersion was combined with 1 mL of EG solution. The mixture was then subjected to irradiation with 10 W UV light, while the transmittance of the

dispersion was continuously monitored in situ using UV-vis-NIR spectroscopy. Data collection were performed at intervals of 1 s.

### Photothermal conversion measurements

The photothermal conversion capability of Fe<sub>1</sub>-TiO<sub>2</sub> nanostructures was evaluated by recording the temperature profile of an EG solution containing 1 wt.% of Fe<sub>1</sub>-TiO<sub>2</sub> nanostructures. Typically, 1 mL of the Fe<sub>1</sub>-TiO<sub>2</sub> dispersion was introduced into 1 mL of EG solution. The mixture was then exposed to simulated sunlight (0.52 W·cm<sup>-2</sup>), and the temperature of the dispersion was continuously monitored in situ using a JK804 multi-channel sensor. Data collection were performed at intervals of 30 s.

### Photothermal catalytic measurements

The photothermal catalytic performance of Fe<sub>1</sub>-TiO<sub>2</sub> was evaluated using polyester glycolysis as a model reaction in the following experimental procedure. First, 1 mL of the Fe<sub>1</sub>-TiO<sub>2</sub> dispersion, 1 mL of EG, and 0.5 g of polyethylene terephthalate (PET) film/powder/tube were added to a 20 mL quartz reactor and sealed. The reactor was then placed under simulated sunlight, and the temperature of the dispersion was monitored by a JK804 multi-channel sensor. The thermal catalysis was heated by an oil bath. When depolymerization is complete, the PET and its oligomers were filtrated, washed, and dried at 80 °C for 24 h. The filtrate was a mixture of the remaining EG, monomer, and distilled water. The conversion of PET was calculated according to the following equations, respectively:

$$\text{Conversion of PET} = \frac{m_0 - m_t}{m_0} \times 100\% \quad (8)$$

In which,  $m_0$  represents the initial weight of PET and  $m_t$  represents the weight of residual PET;  $M_{\text{PET}}$  corresponds to the molecular weight of PET repeating unit (192.2 g·mol<sup>-1</sup>). The bis(2-hydroxyethyl) terephthalate (BHET) was quantitatively analyzed using <sup>1</sup>H NMR spectroscopy at 400-MHz Bruker AVANCE AV III instrument, with d<sup>6</sup>-DMSO as the solution. The dichloromethane signals as internal standard ( $\delta = 5.76$  ppm, 1H), and the representative characteristic signals areas for BHET ( $\delta = 8.13$  ppm, 4H) were calculated to determine the yield of the BHET in the <sup>1</sup>H NMR spectra. The yield of BHET was calculated using the following equations:

$$n_{\text{BHET}} = \frac{A_{\text{BHET}}/N_{\text{BHET}}}{A_i/N_i} * n_i \quad (9)$$

$$\text{Yield of BHET} = \frac{n_{\text{BHET}}}{m_0} * 100\% \quad (10)$$

where  $A_{\text{BHET}}$  and  $N_{\text{BHET}}$  refer to the characteristic signal peak area and protons number of BHET, respectively,  $A_i$  and  $N_i$  denote the characteristic signal peak area and the protons number of the internal standard, respectively,  $n_{\text{BHET}}$  and  $n_i$  refer to the mol of BHET and internal standard.

To investigate the long-term stability of the catalyst more comprehensively, we carried out seven long-term parallel experiments, aiming to simulate extended reaction periods. Each experiment maintained consistency in terms of the number of reactants (10 g PET and 20 g EG), catalyst dosage (2 mg Fe-TiO<sub>2</sub>), light intensity (0.68 W·cm<sup>-2</sup>), and reaction temperature (170 °C). The sole parameter that varied was the reaction time, set at 10, 12.5, 15, 17.5, 20, 22.5, and 25 h, respectively.

### General procedure for photothermal catalytic PC/PLA/PBT glycolysis

First, 1 mL of the Fe<sub>1</sub>-TiO<sub>2</sub> dispersion, 1 mL of EG, and 0.5 g of PC/PLA/PBT films were added to a 20 mL quartz reactor and sealed. The reactor

was then placed under simulated sunlight, and the temperature of the dispersion was monitored by a JK804 multi-channel sensor. After the reaction was completed, the reaction mixture was cooled to room temperature. Taking “polycarbonate (PC)” as an example, unreacted PC films and oligomers were separated by filtration, collected, dried at 80 °C for 24 h, and weighed. The filtrate was a mixture of the remaining EG, monomer. The filtrate was then evaporated by rotary distillation to give a colloidal liquid, which was dissolved in equal volumes of ethyl acetate and distilled water, transferred to a separatory funnel, and shaken vigorously, and the mixture separated into two phases. The upper organic phase was subjected to rotary evaporation to remove the ethyl acetate and dried at 80 °C for 24 h and weighed, which was mainly the product. The special activity of the monomer was calculated according to the following equations, respectively:

$$\text{Activity} = \frac{m_{\text{monomer}}}{m_{\text{catal.}} \times \text{time}} \quad (11)$$

In which,  $m_{\text{monomer}}$ ,  $m_{\text{catal.}}$ , time represent the weight of monomer, the weight of the catalyst, and the reaction time, respectively.

## Data availability

The source data generated in this study are provided in the Source Data file. Source data are provided with this paper.

## References

- Yu, K., Lou, L., Liu, S. & Zhou, W. Asymmetric oxygen vacancies: the intrinsic redox active sites in metal oxide catalysts. *Adv. Sci.* **7**, 1901970 (2019).
- Zhou, Q. et al. Generating dual-active species by triple-atom sites through peroxy monosulfate activation for treating micropollutants in complex water. *Proc. Natl Acad. Sci. USA* **120**, e2300085120 (2023).
- Ma, D. et al. Enhanced catalytic ozonation for eliminating CH<sub>3</sub>SH via stable and circular electronic metal-support interactions of Si–O–Mn bonds with low Mn loading. *Environ. Sci. Technol.* **56**, 3678–3688 (2022).
- Xu, M. et al. Insights into interfacial synergistic catalysis over Ni@TiO<sub>2-x</sub> catalyst toward water-gas shift reaction. *J. Am. Chem. Soc.* **140**, 11241–11251 (2018).
- Zhu, J. et al. Asymmetric triple-atom sites confined in ternary oxide enabling selective CO<sub>2</sub> photothermal reduction to acetate. *J. Am. Chem. Soc.* **143**, 18233–18241 (2021).
- Zhu, S. et al. Selective CO<sub>2</sub> photoreduction into C<sub>2</sub> product enabled by charge-polarized metal pair sites. *Nano Lett.* **21**, 2324–2331 (2021).
- Zhang, P. et al. Mesoporous MnCeO<sub>x</sub> solid solutions for low temperature and selective oxidation of hydrocarbons. *Nat. Commun.* **6**, 8446 (2015).
- Chen, A. et al. Structure of the catalytically active copper-ceria interfacial perimeter. *Nat. Catal.* **2**, 334–341 (2019).
- Xiong, L. et al. Highly selective transformation of biomass derivatives to valuable chemicals by single-atom photocatalyst Ni/TiO<sub>2</sub>. *Adv. Mater.* **35**, 2209646 (2023).
- Pastor, E. et al. Electronic defects in metal oxide photocatalysts. *Nat. Rev. Mater.* **7**, 503–521 (2022).
- Zhao, Y. et al. Tuning oxygen vacancies in ultrathin TiO<sub>2</sub> nanosheets to boost photocatalytic nitrogen fixation up to 700 nm. *Adv. Mater.* **31**, 1806482 (2019).
- George, S. et al. Role of Fe doping in tuning the band gap of TiO<sub>2</sub> for the photo-oxidation-induced cytotoxicity paradigm. *J. Am. Chem. Soc.* **133**, 11270–11278 (2011).
- Liu, P. et al. Photochemical route for synthesizing atomically dispersed palladium catalysts. *Science* **352**, 797–800 (2016).
- Yao, S. et al. Atomic-layered Au clusters on α-MoC as catalysts for the low-temperature water-gas shift reaction. *Science* **357**, 389–393 (2017).
- Liu, C. et al. Oxygen evolution reaction over catalytic single-site Co in a well-defined brookite TiO<sub>2</sub> nanorod surface. *Nat. Catal.* **4**, 36–45 (2020).
- Yao, Y. et al. High temperature shockwave stabilized single atoms. *Nat. Nanotechnol.* **14**, 851–857 (2019).
- Lee, C. W. et al. Photochemical tuning of dynamic defects for high-performance atomically dispersed catalysts. *Nat. Mater.* **23**, 552–559 (2024).
- Liu, K. et al. Strong metal-support interaction promoted scalable production of thermally stable single-atom catalysts. *Nat. Commun.* **11**, 1263 (2020).
- Liu, B. et al. Large-scale synthesis of transition-metal-doped TiO<sub>2</sub> nanowires with controllable overpotential. *J. Am. Chem. Soc.* **135**, 9995–9998 (2013).
- Zhang, Z. et al. Generalized synthetic strategy for transition-metal-doped brookite-phase TiO<sub>2</sub> nanorods. *J. Am. Chem. Soc.* **141**, 16548–16552 (2019).
- Guo, Y. et al. Photo-thermo semi-hydrogenation of acetylene on Pd<sub>1</sub>/TiO<sub>2</sub> single-atom catalyst. *Nat. Commun.* **13**, 2646 (2022).
- Lee, B. et al. Electronic interaction between transition metal single-atoms and anatase TiO<sub>2</sub> boosts CO<sub>2</sub> photoreduction with H<sub>2</sub>O. *Energy Environ. Sci.* **15**, 601–609 (2022).
- Sun, W., Kitchaev, D. A., Kramer, D. & Ceder, G. Non-equilibrium crystallization pathways of manganese oxides in aqueous solution. *Nat. Commun.* **10**, 573 (2019).
- Bianchini, M. et al. The interplay between thermodynamics and kinetics in the solid-state synthesis of layered oxides. *Nat. Mater.* **19**, 1088–1095 (2020).
- Aleisa, R., Feng, J., Ye, Z. & Yin, Y. Rapid high-contrast photo-reversible coloration of surface-functionalized N-doped TiO<sub>2</sub> nanocrystals for rewritable light-printing. *Angew. Chem. Int. Ed.* **61**, e202203700 (2022).
- O’Quinn, E. C. et al. Predicting short-range order and correlated phenomena in disordered crystalline materials. *Sci. Adv.* **6**, eabc2758 (2020).
- Feng, J. et al. Surface-bound sacrificial electron donors in promoting photocatalytic reduction on titania nanocrystals. *Nanoscale* **11**, 19512–19519 (2019).
- Chen, J. et al. Unveiling synergy of strain and ligand effects in metallic aerogel for electrocatalytic polyethylene terephthalate upcycling. *Proc. Natl Acad. Sci. USA* **121**, e2318853121 (2024).
- Farges, F., Brown, G. E. & Rehr, J. J. Ti K-edge XANES studies of Ti coordination and disorder in oxide compounds: comparison between theory and experiment. *Phys. Rev. B* **56**, 1809–1819 (1997).
- Bordiga, S. et al. XAFS study of Ti-silicalite: structure of framework Ti(IV) in the presence and absence of reactive molecules (H<sub>2</sub>O, NH<sub>3</sub>) and comparison with ultraviolet-visible and IR results. *J. Phys. Chem.* **98**, 4125–4132 (1994).
- Yamashita, H. et al. Photocatalytic decomposition of NO at 275 K on titanium oxides included within Y-zeolite cavities: the structure and role of the active sites. *J. Phys. Chem.* **100**, 16041–16044 (1996).
- Wu, Q., Zheng, Q. & van de Krol, R. Creating oxygen vacancies as a novel strategy to form tetrahedrally coordinated Ti<sup>4+</sup> in Fe/TiO<sub>2</sub> nanoparticles. *J. Phys. Chem. C* **116**, 7219–7226 (2012).
- Gaultois, M. W. & Grosvenor, A. P. Coordination-induced shifts of absorption and binding energies in the SrFe<sub>1-x</sub>Zn<sub>x</sub>O<sub>3-δ</sub> system. *J. Phys. Chem. C* **114**, 19822–19829 (2010).
- Jiang, N., Su, D. & Spence, J. C. H. Determination of Ti coordination from pre-edge peaks in Ti K-edge XANES. *Phys. Rev. B* **76**, 214117 (2007).
- Sun, J. W. et al. Scalable synthesis of coordinatively unsaturated metal-nitrogen sites for large-scale CO<sub>2</sub> electrolysis. *Nat. Commun.* **14**, 1599 (2023).

36. Noriega, R. et al. A general relationship between disorder, aggregation and charge transport in conjugated polymers. *Nat. Mater.* **12**, 1038–1044 (2013).
37. Assi, H. et al. Titanium coordination compounds: from discrete metal complexes to metal–organic frameworks. *Chem. Soc. Rev.* **46**, 3431–3452 (2017).
38. Fowles, G. W. A. Lone pair electrons. *J. Chem. Educ.* **34**, 187 (1957).
39. Saglam, H. et al. Entropy-driven order in an array of nanomagnets. *Nat. Phys.* **18**, 706–712 (2022).
40. Lee, B. H. et al. Reversible and cooperative photoactivation of single-atom Cu/TiO<sub>2</sub> photocatalysts. *Nat. Mater.* **18**, 620–626 (2019).
41. Chen, X., Liu, L., Yu, P. Y. & Mao, S. S. Increasing solar absorption for photocatalysis with black hydrogenated titanium dioxide nanocrystals. *Science* **331**, 746–750 (2011).
42. Fang, Y. et al. Dual activation of molecular oxygen and surface lattice oxygen in single atom Cu<sub>1</sub>/TiO<sub>2</sub> catalyst for CO oxidation. *Angew. Chem. Int. Ed.* **61**, e202212273 (2022).
43. Cao, X. et al. A photochromic composite with enhanced carrier separation for the photocatalytic activation of benzylic C–H bonds in toluene. *Nat. Catal.* **1**, 704–710 (2018).
44. Liu, Y. et al. Integrated photochromic-photothermal processes for catalytic plastic upcycling. *Angew. Chem. Int. Ed.* **62**, e20230893 (2023).
45. Cao, X. et al. Engineering lattice disorder on a photocatalyst: photochromic BiOBr nanosheets enhance activation of aromatic C–H bonds via water oxidation. *J. Am. Chem. Soc.* **144**, 3386–3397 (2022).
46. Chen, J. et al. Toward carbon neutrality: selective conversion of waste plastics into value-added chemicals. *Matter* **6**, 3322–3347 (2023).

## Acknowledgements

This work was supported by the National Key Research and Development Program of China (2023YFC3903200 to J.C.), the National Natural Science Foundation of China (22376152 to J.C.), the Suzhou Frontier Technology Research Advanced Materials Project (SYG202305 to J.C.), and Jiangsu Provincial Fund for Excellent Young Scholars (BK20240154 to J.C.). The authors thank the support from Suzhou Key Laboratory of Advanced Photonic Materials, Collaborative Innovation Center of Suzhou Nano Science & Technology, the 111 Project, and TPS (beamline 44A) and SSRF (beamline 11B) for the allocation of synchrotron beamtime. Research at the University of Western Ontario is supported by the Natural Science and Engineering Council of Canada, the Canada Research Chair, and the Canada Foundation for Innovation. J.C. thanks Dr. Wenxiu Yang for the help with the TEM measurements.

## Author contributions

Conceptualization: J.C. and Y.Y.; Methodology: Y.L., X.W., and X.L.; Investigation: Y.L., X.W., X.L., and Z.Y.; Writing—original draft: Y.L., Z.Y., Y.Y., and J.C.; Writing—review and editing: J.C., Y.Y., M.C., T.S., P.X., and Q.Z.; Funding acquisition: J.C.; Supervision: J.C. and Y.Y.

## Competing interests

The authors declare no competing interests.

## Additional information

**Supplementary information** The online version contains supplementary material available at <https://doi.org/10.1038/s41467-024-53774-5>.

**Correspondence** and requests for materials should be addressed to Yadong Yin or Jinxing Chen.

**Peer review information** *Nature Communications* thanks Jianping Yang and the other, anonymous, reviewer(s) for their contribution to the peer review of this work. A peer review file is available.

**Reprints and permissions information** is available at <http://www.nature.com/reprints>

**Publisher's note** Springer Nature remains neutral with regard to jurisdictional claims in published maps and institutional affiliations.

**Open Access** This article is licensed under a Creative Commons Attribution-NonCommercial-NoDerivatives 4.0 International License, which permits any non-commercial use, sharing, distribution and reproduction in any medium or format, as long as you give appropriate credit to the original author(s) and the source, provide a link to the Creative Commons licence, and indicate if you modified the licensed material. You do not have permission under this licence to share adapted material derived from this article or parts of it. The images or other third party material in this article are included in the article's Creative Commons licence, unless indicated otherwise in a credit line to the material. If material is not included in the article's Creative Commons licence and your intended use is not permitted by statutory regulation or exceeds the permitted use, you will need to obtain permission directly from the copyright holder. To view a copy of this licence, visit <http://creativecommons.org/licenses/by-nc-nd/4.0/>.

© The Author(s) 2024